The Effects of Midlatitude Waves over and around the Tibetan Plateau on Submonthly Variability of the East Asian Summer Monsoon

HATSUKI FUJINAMI AND TETSUZO YASUNARI

Hydrospheric Atmospheric Research Center, Nagoya University, Nagoya, Japan

(Manuscript received 16 October 2008, in final form 17 January 2009)

ABSTRACT

Convective variability at submonthly time scales (7–25 days) over the Yangtze and Huaihe River basins (YHRBs) and associated large-scale atmospheric circulation during the mei-yu season were examined using interpolated outgoing longwave radiation (OLR) and NCEP–NCAR reanalysis data for 12 yr having active submonthly convective fluctuation over the YHRBs within the period 1979–2004. Correlations between convection anomalies over the YHRBs and upper-level streamfunction anomalies at every grid point show two contrasting patterns. One pattern exhibits high correlations along the northern to eastern peripheries of the Tibetan Plateau (defined as the NET pattern), whereas the other has high correlations across the Tibetan Plateau (defined as the AT pattern). Composite analysis of the NET pattern shows slow southward migration of convection anomalies from the northeastern periphery of the Tibetan Plateau to southern China, in relation to southward migration of the mei-yu front caused by simultaneous amplification of upper- and low-level waves north of the YHRBs. In the AT pattern, convection anomalies migrate eastward from the western Tibetan Plateau to the YHRBs. A low-level vortex is created at the lee of the plateau by eastward-moving upper-level wave packets and associated convection from the plateau. Rossby wave trains along the Asian jet characterize the upper-level circulation anomalies in the two patterns. The basic state of the Asian jet during the mei-yu season differs between the two patterns, especially around the Tibetan Plateau. The Asian jet has a northward arclike structure in NET years, while a zonal jet dominates in AT years. These differences could alter the Rossby wave train propagation route. Furthermore, the larger zonal wavenumber of AT waves (~7–8) than of NET waves (~6) means faster zonal phase speed relative to the ground in the AT pattern than in the NET pattern. These differences likely explain the meridional amplification of waves north of the YHRBs in the NET pattern and the eastward wave movement across the plateau in the AT pattern.

1. Introduction

Climatologically, the rainy season in China has large seasonal variation, with three high-rainfall periods and locations: a presummer rainy season in mid-May over South China, the mei-yu season over the Yangtze and Huaihe River basins (YHRBs) in central China from mid-June to mid-July, and a summer rainy season in North/Northeast China after mid-July (e.g., Ding 1992; Tian and Yasunari 1998; Ding and Chan 2005). The seasonal variation shows abrupt northward shifts among the three regions, associated with abrupt seasonal changes in large-scale atmospheric circulation over East Asia (e.g., Ueda and Yasunari 1996).

In the mei-yu season, a quasi-stationary front (called the mei-yu front in China and the baiu front in Japan) is frequently observed in the synoptic weather map, extending from the southeastern edge of the Tibetan Plateau to the east of Japan. Once the front appears over East Asia, the location of the east–west elongated cloud zone (i.e., mei-yu–baiu front) changes very slowly, although mesoscale precipitation systems often move eastward along it.

The mei-yu–baiu front is an important cloud and precipitation system of the East Asian monsoon, providing large amounts of precipitation in early summer. The front forms as a subtropical front under the influence of atmospheric circulation in both the midlatitudes and subtropical–tropical monsoon regions (Ninomiya 1984). The frontal zone corresponds to areas of a large meridional moisture gradient, and moisture transported from the South Asian and western North Pacific monsoon regions plays an important role in maintaining the

Corresponding author address: Dr. Hatsuki Fujinami, Hydrospheric Atmospheric Research Center, Nagoya University, Furo-cho, Chikusa-ku, Nagoya 464-8601, Japan.
E-mail: hatsuki@hyarc.nagoya-u.ac.jp

DOI: 10.1175/2009MWR2826.1

© 2009 American Meteorological Society

mei-yu–baiu front. Although the mei-yu and baiu systems have common features, their associated atmospheric structures are not identical. Over the YHRBs, the atmospheric structure shows a weak meridional temperature gradient and strong horizontal wind shear in the lower troposphere, whereas areas around the East China Sea and Japan are characterized by large meridional temperature gradients (Ninomiya and Muraki 1986; Ding 1992; Ding and Chan 2005).

Heavy rainfalls during the mei-yu period are mainly generated by meso-α- and meso-β-scale disturbances that are embedded on, and propagate along, the mei-yu front. Meso-α-scale convective systems of the mei-yu period may be classified broadly into two types: the Yangtze River Valley shear line and the low-level vortex (Chen 2004; Ding and Chan 2005). A low-level vortex often occurs over the eastern flank of the Tibetan Plateau. A low-level vortex originating over the Tibetan Plateau sometimes moves eastward and triggers the vortex when it moves off the plateau (Tao and Ding 1981; Wang 1987; Wang and Orlanski 1987; Yasunari and Miwa 2006). The vortex develops and is maintained mainly by latent heating due to strong convection (Wang and Orlanski 1987; Wang et al. 1993).

The convection activity over the YHRBs exhibits substantial intraseasonal variability during the mei-yu period. Intraseasonal oscillations (ISOs) on so-called submonthly (~6–25 days; e.g., Vincent et al. 1998) and Madden–Julian oscillation (MJO; 30–60 days; e.g., Madden and Julian 1972, 1994) time scales strongly control the activity of convections over the YHRBs and South China Sea during the summer monsoon. Previous studies have noted a relationship between ISOs in convection over the YHRBs and those over the South China Sea (Fukutomi and Yasunari 1999; Fukutomi and Yasunari 2002; Chen et al. 2000; Zhu et al. 2003; Mao and Chan 2005). Chen et al. (2000) reported that both 12–24-day and 30–60-day ISOs of convection tend to fluctuate out of phase between the two regions from May to August. When convection is active (suppressed) over the YHRBs and suppressed (active) over the South China Sea, an anticyclonic (cyclonic) circulation anomaly appears in the lower troposphere over the South China Sea. The anticyclonic (cyclonic) anomaly accompanies westerly–southwesterly (easterly–northeasterly) wind anomalies to its north, indicating that an increase (decrease) in moisture supply to the YHRBs from the south is associated with active (suppressed) YHRB convection. Submonthly-scale convection anomalies originate from the western North Pacific and propagate westward over the South China Sea in the early summer, accompanied by low-level circulation anomalies (Fukutomi and Yasunari 1999; Fukutomi and Yasunari 2002; Mao and Chan 2005).

During the northern summer, ISOs also dominate in the extratropics (e.g., Ambrizzi et al. 1995; Terao 1998; Fujinami and Yasunari 2004, hereafter FY04). Quasi-stationary Rossby waves occur in the Asian subtropical jet with periods of ~14 and 30–45 days (Terao 1998). These waves, called the "Silk Road pattern," follow the waveguide for Rossby waves (Terao 1998; Enomoto et al. 2003). FY04 revealed that 7–20-day convective fluctuation over and around the Tibetan Plateau during July and August is strongly controlled by Rossby waves along the Asian jet.

The mei-yu front includes both tropical and extratropical variations because of its geographical location. Therefore, tropical and extratropical interactions are an inherent property of the variation (Hsu 2005). Mao and Wu (2006) examined the ISO of rainfall over the YHRBs during the mei-yu season and related atmospheric circulation for the summer of 1991. An ISO of 15–35 days was dominant in 1991; however, this ISO time scale is not typical over the YHRBs. The low-level troposphere has an anomalous anticyclone (cyclone) appearing from the northern South China Sea to the Philippine Sea in the active (break) phase, whereas the upper-level troposphere is characterized by an anomalous anticyclone (cyclone) over eastern China and an anomalous cyclone (anticyclone) over the northern Tibetan Plateau. The coupled anomalous circulation pattern between the lower and upper troposphere favors large-scale ascending (descending) motion, and hence enhanced (reduced) rainfall over the YHRBs.

However, previous studies have not examined the detailed spatial and temporal evolution of large-scale convection and the structure of atmospheric circulation associated with ISOs of convection over the YHRBs during the mei-yu season. The effects of midlatitude waves (e.g., Rossby waves) along the Asian westerly jet and of the Tibetan Plateau on mei-yu activity also remain poorly understood. During boreal summer, midlatitude systems that vary on submonthly time scales favorably propagate along the Asian westerly jet (e.g., FY04). Thus, a close connection between midlatitude systems and mei-yu variability in early summer could be expected. Therefore, based on the submonthly convective fluctuations over the YHRBs during the mei-yu season, we examined the spatiotemporal evolution of convection and circulation over East Asia, focusing on the relationship between upper-level atmospheric circulation in the midlatitudes and convection over the YHRBs.

In section 2, we describe the data and data processing. In section 3, we present the general characteristics of mean convective activity and atmospheric circulation during the mei-yu period. Time series analysis is also included to demonstrate the interannual variability of submonthly-scale ISO (SISO) of convection over the

YHRBs and to reveal dominant periods of active SISO years based on wavelet analysis. In section 4, we present composite analysis results for active years of SISO to reveal the space–time evolution of the large-scale convection and circulation associated with submonthly-scale convective fluctuation over the YHRBs. Case studies are also shown to clarify how the midlatitude waves affect real weather systems on submonthly time scales over the YHRBs. In section 5, we discuss effects of background time-mean flows on the propagation route of midlatitude waves and the role of the Tibetan Plateau in submonthly-scale convection over the YHRBs. Finally, in section 6, we summarize the results.

2. Data and processing

Interpolated outgoing longwave radiation (OLR) data produced by the National Oceanic and Atmospheric Administration/Climatic Diagnostics Center (NOAA/CDC) are used as a proxy for convection (Liebmann and Smith 1996). National Centers for Environmental Prediction–National Center for Atmospheric Research (NCEP–NCAR) reanalysis data represent large-scale circulation and include zonal and meridional wind components (u, v) (Kalnay et al. 1996). Both types of data include daily averages for the 26-yr period (1979–2004) at global coverage on a 2.5° latitude–longitude grid. Streamfunction (ψ) and divergence were calculated from the wind data using a spectral transform method. Gauge-based analysis data of daily precipitation on a 0.5° latitude–longitude grid over East Asia were also used for a case study (Xie et al. 2007).

Climatologically, circulation fields change abruptly before and after the mei-yu period (10 June–10 July; Ding 1992; Ding and Chan 2005). The different mean basic state probably affects the development and structure of disturbances over the YHRBs and associated large-scale circulation (e.g., Matthews and Kiladis 1999a,b; Fukutomi and Yasunari 2002). Therefore, data during the climatological mei-yu period were extracted to examine the features of SISO over the YHRBs.

Daily anomalies of OLR and the reanalysis data were computed by subtracting the first three harmonics of the annual cycle (about 120 days) at each grid point for each year. Submonthly (7–25 day) perturbations were then computed by applying a Lanczos filter (Duchon 1979) to the detrended anomalies.

3. Submonthly convective variability over the Yangtze and Huaihe River basins

a. Large-scale mean conditions

Figure 1 shows the climatological structure of convective activity and atmospheric circulation, based on the 26-yr average during the mei-yu period. A zonally elongated, banded active convection zone (OLR < 230 W m^{-2}) is observable from East China to Japan, corresponding to the mei-yu–baiu frontal zone (Fig. 1a). The frontal zone is accompanied by strong low-level southwesterlies. Deep convections (OLR < 200 W m^{-2}) extend over the Bay of Bengal, Indochina Peninsula, and to the west of the Philippines. Active convection also appears over the southeastern part of the Tibetan Plateau. A subtropical anticyclone broadly covers the western North Pacific, where convection is suppressed. In the upper troposphere, an upper-level anticyclone

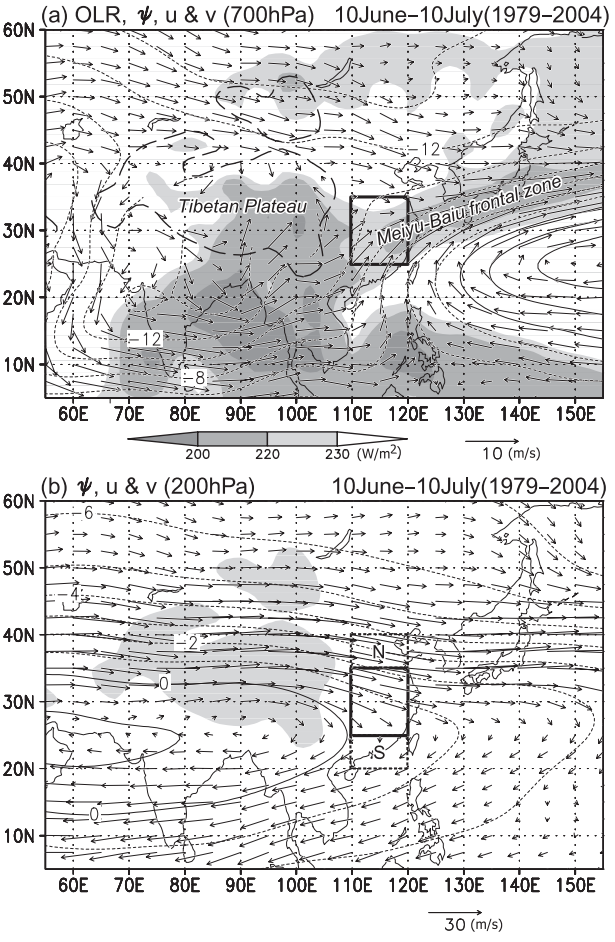

FIG. 1. (a) Mean OLR (shading), 700-hPa streamfunction (ψ), and wind vectors for the mei-yu period (10 June–10 July) 1979–2004. The contour interval for ψ is 2×10^6 m^2 s^{-1}. The topographic contour line for 1500 m is also shown (thick dashed line). The key convective variation region is enclosed by the 25°–35°N, 110°–120°E grid box. (b) Same as (a), but for the 200-hPa streamfunction (ψ) and wind vectors. Two rectangular domains, labeled N (35°–40°N, 110°–120°E) and S (20°–25°N, 110°–120°E), are indicated by dotted lines (as explained in the text). The contour interval is 1×10^7 m^2 s^{-1}. Shading denotes areas higher than 1500 m in surface altitude.

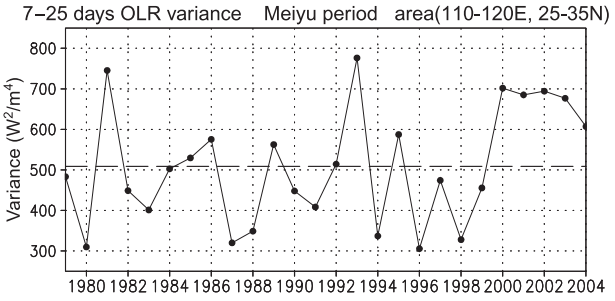

FIG. 2. Interannual variation of 7–25-day OLR variance over the key region (25°–35°N, 110°–120°E) during the mei-yu period (10 June–10 July). The dashed line denotes the 26-yr mean of the variance (508.7 W^2 m^{-4}).

(Tibetan high) is evident south of the Tibetan Plateau (Fig. 1b). To the north of the Tibetan high, the Asian westerly jet lies along the jet axis at approximately 37.5°N.

b. Characteristics of submonthly-scale convective variability during the mei-yu period

The boxed region (25°–35°N, 110°–120°E) in Fig. 1a is treated as a key region for the detailed examination of submonthly-scale convective fluctuation over the YHRB. The region includes active convection over East China and is characterized as a convergence zone along the low-level strong southwesterly flow and a shallow upper-level trough (Figs. 1a,b). Figure 2 shows the interannual variation of 7–25-day OLR variance over the key region during the mei-yu period. The variance exhibits large interannual variation from 1979 to 1999, whereas large variance persists after 2000 with no clear interannual variation. In years of suppressed SISO, we found ISOs of approximately 30 days (e.g., 1988, 1991, 1994, and 1998) and less remarkable ISOs of both submonthly and longer time scales (e.g., 1980, 1983, 1987, 1996; data not shown). Hereafter, we scrutinize active SISO years (12 yr: 1981, 1985, 1986, 1989, 1992, 1993, 1995, 2000, 2001, 2002, 2003, and 2004), characterized by variance exceeding the 26-yr mean value (508.7 W^2 m^{-4}; dashed line in Fig. 2), to show typical SISO features over the YHRBs.

We applied wavelet analysis (Torrence and Compo 1998) to the detrended OLR time series, averaged over the key region for the active SISO years. To avoid redundancy, the wavelet spectra are presented only for 1992 and 1993, the years with the minimum and maximum submonthly variance, respectively, among the 12 yr (Fig. 2). In both years, submonthly variations are dominant during the climatological mei-yu period, reflecting the appearance of the mei-yu front. The 1992 OLR anomalies have quasi-periodic oscillation with three active convection phases during the mei-yu period (Fig. 3a). The active phases include large and continuous precipitation (~10–20 mm day^{-1}). The wavelet spectrum shows a statistically significant peak with a period of approximately 7–12 days during the mei-yu period (Fig. 3b). In 1993, the detrended OLR anomalies also exhibit remarkable intraseasonal variation, but larger amplitude than in 1992. The wavelet spectrum has a significant peak in an 8–25-day period range during the mei-yu period (Fig. 3d). In the other years, except for 2002, statistically significant (at the 95% level) peaks are evident in a submonthly (7–25 day) range

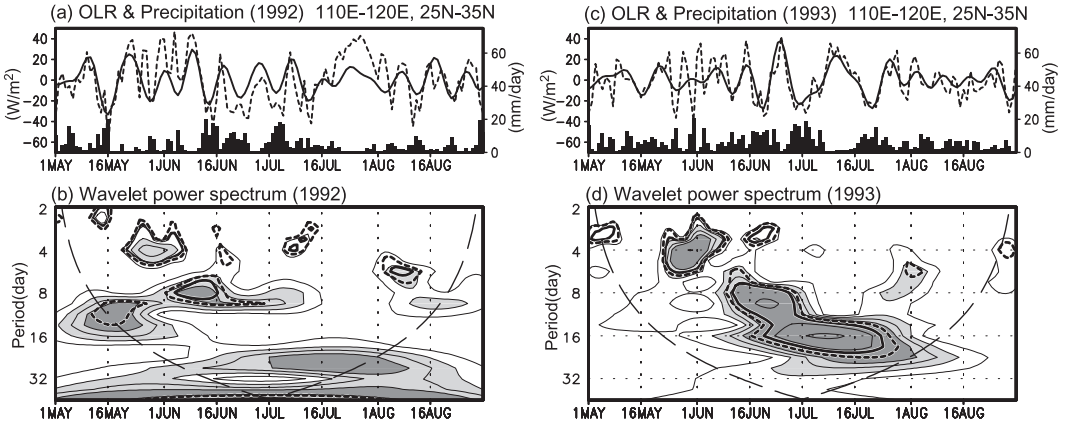

FIG. 3. (a) Time series of detrended OLR anomalies (dashed line), 7–25-day filtered anomalies (solid line), and unfiltered precipitation (black bar) averaged over the key region for 1992. (b) The local wavelet power spectrum of the detrended 1992 OLR anomalies, normalized by $1/\sigma^2$ [$\sigma^2 = 556.4$ (W m^{-2})^2]. The contours are at 1, 2, 3, 4, 8, and 12. Heavy shading denotes areas with power values >4, whereas light shading denotes areas between 2 and 4. The thick solid (dotted) contour line encloses regions of >95% (90%) confidence for a red noise process with a lag 1 coefficient. The dashed line indicates the cone of influence outside of which edge effects become important. (c),(d) As in (a),(b), respectively, but for 1993. The power is normalized by $1/\sigma^2$ [$\sigma^2 = 331.6$ (W m^{-2})^2].

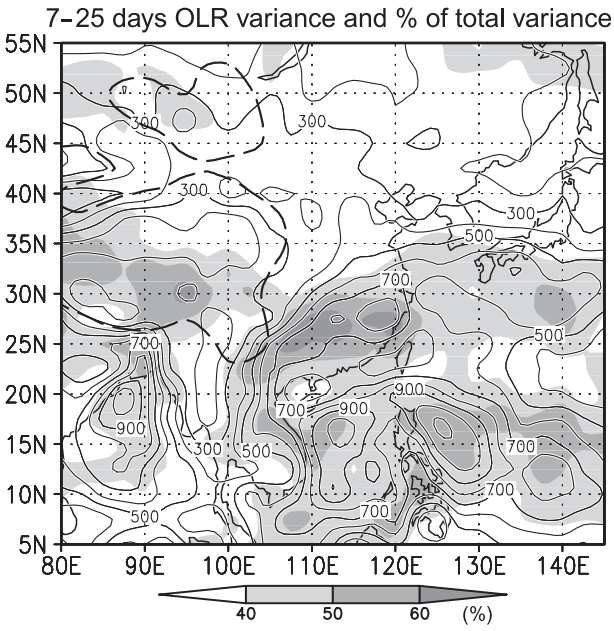

FIG. 4. The 7–25-day OLR variance (contours) and the percentage it composes of total variance (shading) during the mei-yu period (10 June–10 July) for active SISO years (e.g., 1981, 1985, 1986, 1989, 1992, 1993, 1995, 2000, 2001, 2002, 2003, and 2004). The contour interval is 100 $(\mathrm{W\ m^{-2}})^2$. The thick dashed line indicates the topographic contour line for 1500 m.

within the mei-yu period (not shown). Thus, submonthly oscillation was the dominant mode during the mei-yu period in these years.

Figure 4 presents the 12-yr mean structure in variance and the percentage variance of the 7–25-day filtered OLR. A zonal distribution of high variance (>600 $\mathrm{W^2\ m^{-4}}$), extending from South China to the western part of Japan, corresponds to the mei-yu–baiu frontal activity (Fig. 1a). There is a local maximum of variance exceeding 700 $\mathrm{W^2\ m^{-4}}$ within the key region. The key region overlaps the percentage of total variance exceeding 50%–60%. High values up to 900 $\mathrm{W^2\ m^{-4}}$ are located over the Bay of Bengal, the South China Sea, and the Philippine Sea. Areas exceeding 50% of the percentage variance are also seen over the southern Tibetan Plateau, the northeastern part of the Indochina Peninsula, the north South China Sea, and the Philippine Sea, suggesting a possible relationship in submonthly convective variability between the YHRBs and these regions.

4. Spatial structure and temporal evolution

a. Two contrasting relationships between convection and upper-level circulation

In this section, we examine the temporal variation in convection and circulation associated with submonthly convective fluctuations over the YHRBs, based on a time composite analysis. Before the composite analysis, the relationship between convection over the YHRBs and upper-level atmospheric circulation was investigated. In the upper-level atmosphere, there is a large meridional pressure gradient between regions to the north (N region) and south (S region) of the key region, as shown in Fig. 1b. Active convection associated with mei-yu frontal activity generally occurs along the southern side of the upper-level westerly jet, where upper-level divergence dominates (Figs. 1a,b). It is expected that midlatitude waves propagating along the jet could change upper-level wind fields by varying the upper-level meridional pressure gradient and divergence fields over the YHRBs. This, in turn, could influence the mei-yu frontal activity (e.g., FY04). Therefore, we focus on the relationship between convection over the YHRBs and upper-level atmospheric circulation in the N and S regions. Figure 5a is a scatter diagram of the correlation coefficients between 7–25-day OLR anomalies averaged over the key region and 7–25-day 200-hPa streamfunction anomalies in the N and S regions for each of the 12 yr. The largest absolute correlation coefficient within each region (15 grids) is plotted for each year. In the S region, OLR anomalies correlate negatively with the 200-hPa streamfunction (ψ_{200}) anomalies, except in 2000 and 2002. In contrast, in the N region, the signs of the correlation coefficients vary from year to year. Based on the sign of the correlation in the N region, we roughly classified these years (except 2000 and 2002) into two types: positive-correlation years (e.g., 1981, 1985, 1989, 1992, and 2004; closed circles in Fig. 5a) and negative-correlation years (e.g., 1986, 1993, 1995, 2001, and 2003; open circles in Fig. 5a). The negative-correlation years include weak-correlation years in the N region (e.g., 1986). However, a remarkable difference between the positive- and negative-correlation years is whether positive correlation exists in the N region. Therefore, we used the year to examine the general features of positive- and negative-correlation years. This does not alter the following results for negative-correlation years. Figures 5b,c show the spatial distribution of the correlation coefficients between the YHRB OLR anomalies and ψ_{200} anomalies in every grid for the two types. We assembled the filtered OLR anomalies averaged over the key region and ψ_{200} anomalies in every grid during the mei-yu period in the positive- and negative-correlation years, respectively, following the sequential order of the years to make a new dataset (155 days). The correlation coefficient patterns in Figs. 5b,c were constructed using the newly formed time series. In the positive-correlation years (Fig. 5b), large values extend from the northern to

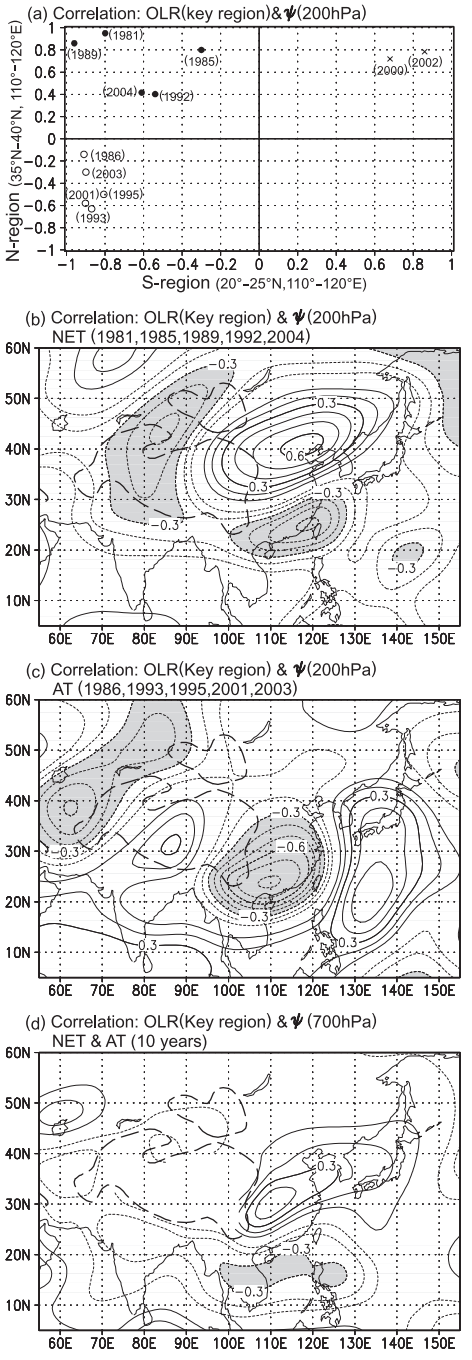

FIG. 5. Scatter diagram of the correlation coefficient between 7–25-day OLR anomalies over the key region and 7–25-day 200-hPa streamfunction (ψ) anomalies in the N and S regions for the active SISO years. Filled and open circles denote years of NET and AT patterns, respectively. (b) Correlation coefficients between OLR anomalies over the key region and 200-hPa ψ anomalies in every grid in the 7–25-day bands for the NET pattern. The contour interval is 0.1. The zero contour line is not plotted. Areas that have correlation coefficients < -0.3 are shaded. (c) As in (b), but for the AT pattern. (d) As in (b),(c), but for 700-hPa ψ anomalies for both the NET and AT patterns. See the text for an explanation of the correlation coefficient calculation.

the eastern peripheries of the Tibetan Plateau (hereafter defined as the NET pattern); there is a high positive correlation (more than 0.6) around 40°N, 115°E, but a negative correlation (less than −0.6) centered on 25°N, 120°E. Correlations larger than ~0.2 are significant at the 99% level in Figs. 5b–d. Active (suppressed) convections over the YHRBs are associated with an anomalous trough (ridge) to the north of the YHRBs and anomalous ridge (trough) to the south of the YHRBs in the upper troposphere. However, in the negative-correlation years (Fig. 5c), high correlation coefficients appear along approximately 30°N across the Tibetan Plateau with a wave train–like distribution (hereafter defined as the AT pattern); the entire key region has negative correlations. Active (suppressed) convections over the YHRBs are associated with the upper-level anomalous ridge (trough). The two types of correlation coefficient patterns suggest that the dominant processes inducing SISO in mei-yu activity are different even though they have the same submonthly time scales. Therefore, we performed composite analysis separately for years with NET and AT patterns. For 2000, the correlation pattern was similar to that for the AT pattern, but the overall pattern was shifted westward by about 10° relative to that for the AT pattern (not shown). In 2002, the correlation distribution showed a wavelike structure from the head of the Bay of Bengal to the east of Japan (not shown), and positive correlations extended broadly from northern China to east of Taiwan, including the YHRBs.

Figure 5d is the same as Figs. 5a,b, but for 700-hPa streamfunction (ψ_{700}) anomalies. The data for both NET and AT pattern years are assembled together (310 days) because overall correlation distributions in both pattern years resemble each other in the key region. Correlation coefficients tend to show opposite signs between the YHRBs and areas to their south including the Indochina Peninsula, the South China Sea, and the Philippine Sea. Active (suppressed) convection over the YHRBs is associated with low-level cyclonic (anticyclonic) circulation over the YHRBs and anticyclonic (cyclonic) anomalies from the Indochina Peninsula to the north of the Philippines, indicating the enhancement of southwesterly (northeasterly) anomalies over the YHRBs. One difference between the two patterns is that significant positive correlations (~0.2) in NET years spread more northward (to 45°N) than those in Fig. 5d, centered on 32.5°N, 112.5°E. In AT years, significant positive correlations are confined between 25° and 35°N and centered on 30°N, 110°E. South of the YHRBs, the NET years show a zonal distribution of significant negative correlations from 90° to 130°E with a single center on the South China Sea, whereas the AT

TABLE 1. Dates of the selected maximum (phase 3) and minimum (phase 7) OLR indices in the key region (25°–35°N, 110°–120°E) in NET and AT years. SF and L indicate a stationary front and a low over the key region, respectively, according to a surface weather chart for day − 1 and day + 1 of the date of the minimum OLR indices. SF+L indicates that a low is embedded on a stationary front.

NET				AT			
Yr	Max OLR (phase 3)	Min OLR (phase 7)		Yr	Max OLR (phase 3)	Min OLR (phase 7)	
1981	—	10 Jun	L	1986	15 Jun	20 Jun	SF+L
1981	15 Jun	26 Jun	SF+L	1986	25 Jun	3 Jul	SF+L
1981	5 Jul	10 Jul	SF	1986	8 Jul	—	—
1985	28 Jun	3 Jul	SF	1993	—	11 Jun	L
1989	—	18 Jun	SF+L	1993	15 Jun	20 Jun	SF+L
1989	23 Jun	28 Jun	SF	1993	25 Jun	30 Jun	SF+L
1989	5 Jul	10 Jul	SF	1993	10 Jul	—	—
1992	—	14 Jun	SF+L	1995	11 Jun	15 Jun	SF+L
1992	18 Jun	23 Jun	SF+L	1995	19 Jun	23 Jun	SF+L
1992	28 Jun	3 Jul	SF+L	1995	27 Jun	3 Jul	SF+L
1992	7 Jul	—	—	2001	—	10 Jun	SF+L
2004	10 Jun	14 Jun	SF	2001	15 Jun	20 Jun	SF+L
2004	19 Jun	23 Jun	SF+L	2003	17 Jun	24 Jun	SF+L
2004	28 Jun	—	—	2003	2 Jul	9 Jul	SF+L

years show a more zonally elongated structure of negative correlations with local minima over the western Tibetan Plateau, India, the Indochina Peninsula, and the Philippine Sea.

b. Composite procedure

We used time composite techniques to establish the relationships between convections over the YHRBs and large-scale atmospheric conditions in years of NET and AT patterns. To create the composites, we selected 12 active and 11 break peaks from the 7–25-day OLR time series for the NET pattern and 12 active and 12 break peaks for the AT pattern (Table 1). According to a surface weather chart, 22 active peaks (total of 24 samples) were accompanied by a stationary front (i.e., the mei-yu front) over the key region. In addition, 17 of the 22 active cases had a low embedded on the front. Thus, composite variations based on the selected samples represent mei-yu frontal activities. As described in the *Glossary of Meteorology* published by the American Meteorological Society (see online at http://amsglossary.allenpress.com/glossary; Glickman 2000), a front that is moving at less than approximately 5 kt (2.6 m s^{-1}) is generally considered quasi-stationary. In synoptic weather analysis, a quasi-stationary front is defined as one that has not moved appreciably from its position on the last previous synoptic chart (e.g., from 3 or 6 h previously). Thus, a ''quasi-stationary front'' means that the front changes little in position as a snapshot. Here we define stationary or quasi-stationary to mean little change in position compared to the previous time or phase. Hence, quasi-stationary phenomena (i.e., fronts, wave trains) may vary on submonthly time scales.

For all the samples, standard deviations exceed the mean of the active SISO years (May–August) by 0.8 (11.5 W^2 m^{-4}), except for three break samples. The standard deviations of composite active and break peaks exceed 1.5 (21.6 W^2 m^{-4}) for both NET and AT patterns. Each cycle was divided into eight different phases, as done by FY04 and Mao and Chan (2005). Phases 3 and 7 correspond to the inactive and active extremes of the YHRBs convection. The mean time span between two subsequent phases was ~1.5 days in both the NET and AT patterns, because the composite cycle was ~12 days. Composite fields were created for each phase. The statistical significance of the composite results at each grid was estimated using Student's *t* tests.

c. NET pattern

Figure 6 illustrates the relationships of convections over the YHRBs, atmospheric circulation, and convective activity from phases 5 to 8 of the NET pattern using composite maps of 7–25-day filtered OLR, wind vectors, and streamfunction (ψ) anomalies. The anomaly structures of phases 1–4 are nearly the same as those from phases 5 to 8, but of opposite sign. Therefore, only phases 5–8 are illustrated, including the transition from inactive to active convection over the YHRBs.

The left-hand panels (Figs. 6a–d) show composites of convection and 700-hPa wind vector and streamfunction (ψ_{700}) anomalies. A notable feature of the phase sequence is the southward movement of active convection anomalies (dark shading) from areas to the northeast of the Tibetan Plateau (around 38°N, 115°E) to South China with a mean speed of 2.6 m s^{-1}, having a zonal

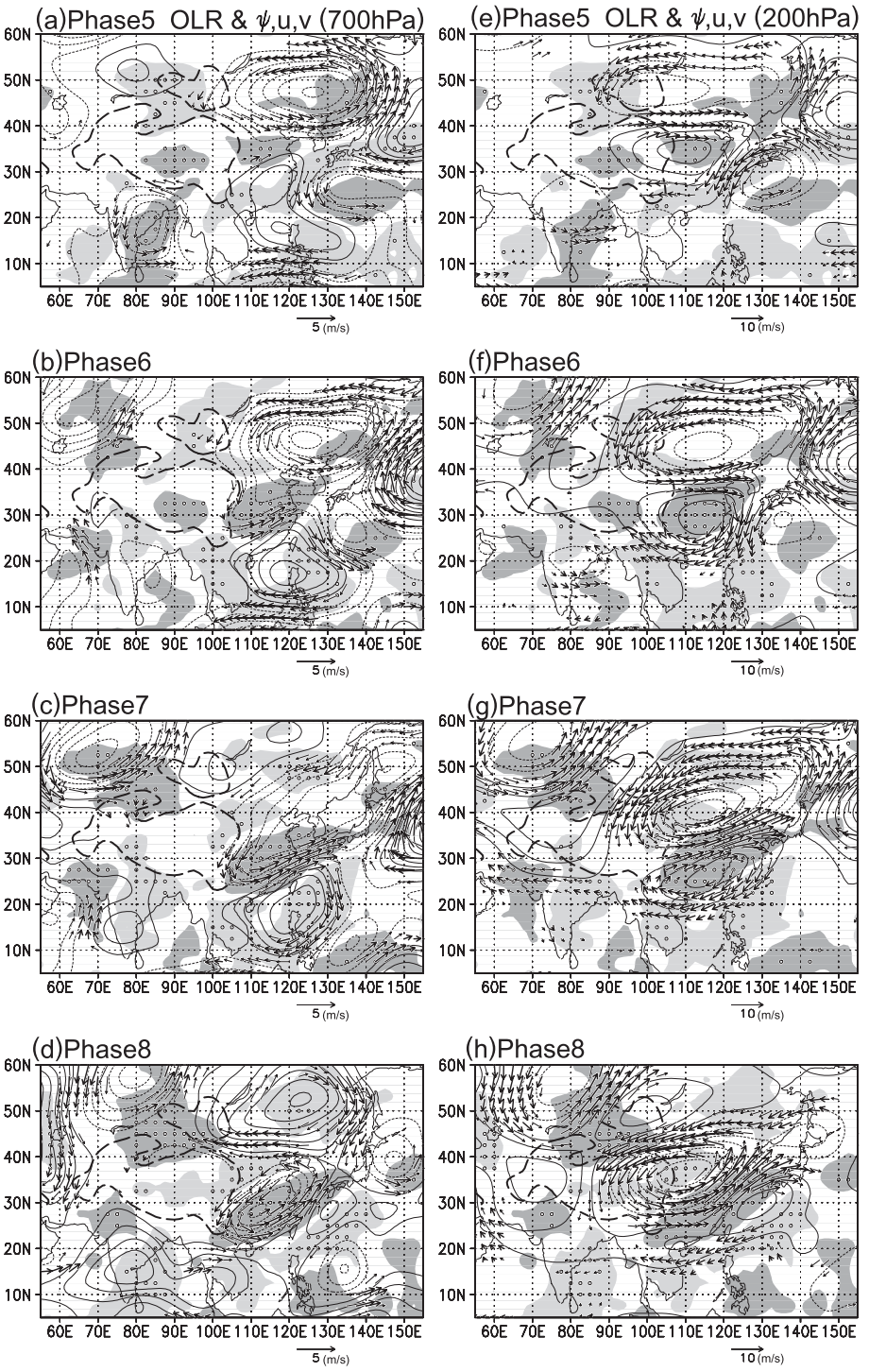

FIG. 6. (a)–(d) Composites of 7–25-day OLR, 700-hPa wind vectors, and streamfunction (ψ) anomalies from phases 5 to 8 for the NET pattern. OLR anomalies less (greater) than -5 (5) W m^{-2} are represented by dark (light) shading. Open circles indicate locally statistically significant grids at the 95% confidence level for the OLR anomalies. Solid (dashed) contours represent positive (negative) ψ values. Zero contours are omitted. The contour interval is 3.0×10^5 m^2 s^{-1}. Only 95% (90%) statistically significant vectors are indicated as thick (thin) solid arrows. The thick dashed line indicates the topographic contour line for 1500 m. (e)–(h) As in (a)–(d), respectively, but for 200 hPa. The contour interval for the streamfunction anomalies is 1.0×10^6 m^2 s^{-1}.

southwest–northeast tilt. In phase 5 (Fig. 6a), an active convection anomaly appears northeast of the Tibetan Plateau. A closed cyclonic circulation anomaly is centered on 45°N, 125°E, and an anticyclonic circulation anomaly extends from southern China to the northern Philippines. Northwesterly wind anomalies in the southwestern flank of the cyclonic anomaly and preexisting southwesterly wind anomalies in the northwestern part of the anticyclonic circulation anomalies converge to the northeast of the Tibetan Plateau, initiating convections there. A similar initiation process was proposed by Takahashi (2003), who examined the southward migration of the mei-yu front in 1992. By phase 6 (Fig. 6b), the active convection signal has moved southward and developed over the YHRBs. The main cyclonic circulation anomaly remains around 45°N, 125°E but spreads southward locally into the key region. Associated with the southwestward extension of the cyclonic circulation anomaly, the anticyclonic circulation anomaly over southern China in the previous phase has moved southward and developed over the northern Philippines. This circulation structure induces enhanced southwesterly wind anomalies over the southern part of the key region, enhancing the transport of abundant moisture into the active convection region. In phase 7 (Fig. 6c), YHRBs convections reach a maximum and tilt zonally to the southwest–northeast, accompanying strong southwesterly wind anomalies to the south. The anticyclonic circulation anomalies centered on the Philippines during phases 6–7 are associated with suppressed convection anomalies over the Philippine Sea and the Indochina Peninsula. Circulation anomalies over the YHRBs have an opposite sign from those over the South China Sea and the Philippine Sea, as noted by Chen et al. (2000). From phases 7 to 8, the OLR anomaly pattern exhibits a zonally tilted tripole structure with positive anomalies in areas northeast of the Tibetan Plateau and from the Indochina Peninsula to the south of Japan, with negative anomalies over the YHRBs. Circulation structures change dramatically in the midlatitudes in phase 8 (Fig. 6d), and ψ_{700} anomalies acquire the sign opposite that in phase 5. An anticyclonic anomaly develops rapidly, centered on 50°N, 120°E, with easterly wind anomalies to its south. Northeasterly wind anomalies become dominant over the northern part of the YHRBs because of a closed cyclonic circulation anomaly over the YHRBs. The circulation structure provides a low-level divergence around 38°N, 110°E, northeast of the Tibetan Plateau, where convection is suppressed. Subsequently, the suppressed convection moves southward to South China from phases 8 to 4, accompanied by a low-level anticyclonic circulation anomaly.

The right-hand panels (Figs. 6e–h) show the same composite, but for 200-hPa wind vector and streamfunction (ψ_{200}) anomalies. Upper-level circulation anomalies associated with submonthly convection signals over the YHRBs spread to the north of 20°N. In addition, as anticipated from Fig. 5a, circulation anomalies of large amplitude appear from the northern to eastern peripheries of the Tibetan Plateau. The composite sequence shows that a cyclonic circulation anomaly north of the key region has quasi-stationary behavior from phases 5 to 8, developing and moving very slowly south-southeastward. In phase 5 (Fig. 6e), a zonally banded cyclonic circulation anomaly extends along 48°N from 90° to 130°E, whereas an anticyclonic circulation anomaly is observable to its south, east of the Tibetan Plateau. The vertical structure of the circulation anomalies is characterized by nearly barotropic structure to the north of 40°N. The simultaneous enhancement of cyclonic circulation in the low- and upper-level troposphere north of the key region triggers subsequent active convection over the key region. In phase 6 (Fig. 6f), a cyclonic circulation anomaly develops rapidly around 55°N, 65°E. The development affects the behavior of circulation anomalies on the downstream side in the subsequent phases. From phases 6 to 8, an anticyclonic circulation anomaly develops from the southern to eastern sides of the upstream cyclonic circulation anomaly. Associated with this, the cyclonic circulation anomaly northeast of the Tibetan Plateau seen in phase 6 moves slightly southeastward and gains strength. Thus, circulation anomalies appear to grow downstream, implying Rossby wave energy propagation to the east. In phase 7 (Fig. 6g), the anomaly structure around the Tibetan Plateau is quite similar to the correlation pattern (Fig. 5b), but with opposite sign. Active convection anomalies over the YHRBs lie along the southeastern flank of the upper-level anomalous cyclone, where southwesterly winds dominate. The anomaly structure is fairly similar to that shown by Mao and Wu (2006, their Fig. 6h), although the dominant periods of the ISOs are not similar. By phase 2, the circulation anomaly over the western Tibetan Plateau acquires a sign opposite to that in phases 7 and 8 (not shown). A cyclonic circulation anomaly develops rapidly near 40°N, 75°E, with the downstream development of anticyclonic circulation centered on 40°N, 110°E.

Figure 7 illustrates the composites of total OLR and circulation fields of inactive and active extremes of YHRB convection. In phase 3, suppressed convection extends broadly from northern to southern China, where a low-level anticyclone dominates (Fig. 7a). This anticyclone is not part of the subtropical anticyclone that brings fine weather after the mei-yu period. Active

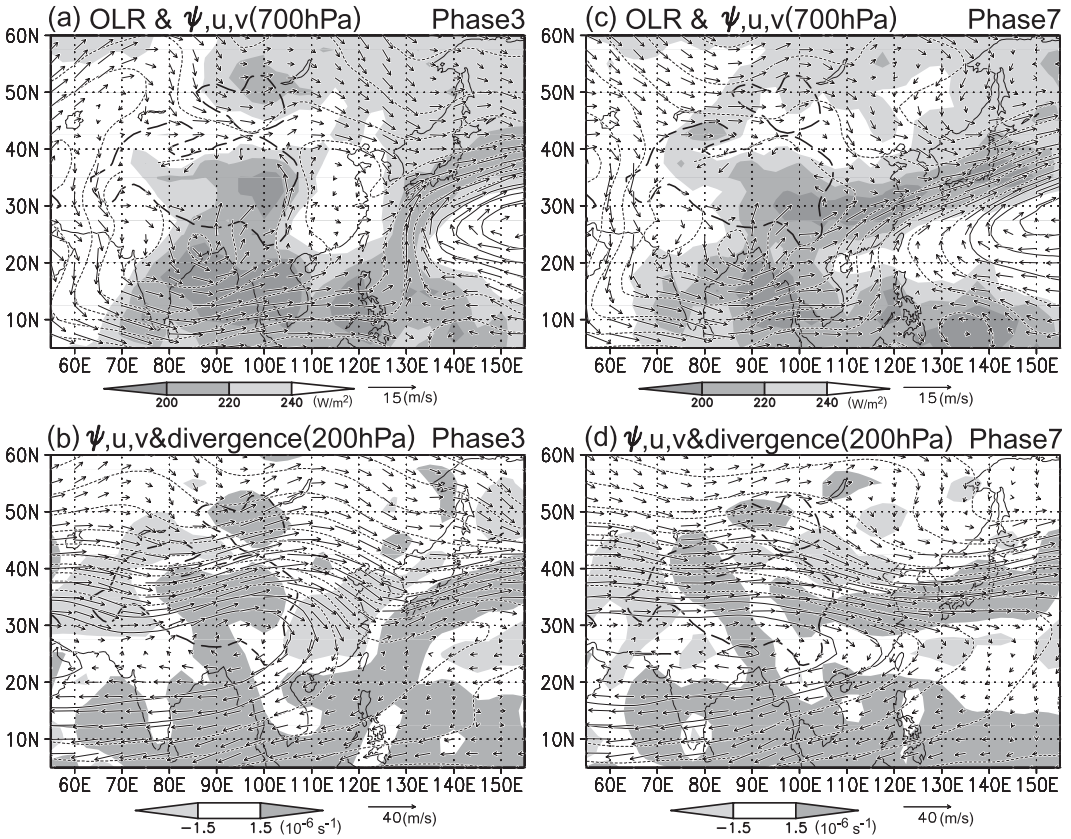

FIG. 7. Composites of (a) total OLR (shading), 700-hPa streamfunction (ψ), and wind vectors at phase 3 in the NET pattern. The contour interval for ψ is 2×10^6 m^2 s^{-1}. The thick dashed line indicates the topographic contour line for 1500 m. (b) As in (a), but for the total 200-hPa streamfunction (ψ) and wind vectors. Shading denotes the total 200-hPa divergence (10^{-6} s^{-1}). The contour for (ψ) is 6×10^6 m^2 s^{-1}. (c),(d) As in (a) and (b), respectively, but for phase 7.

convections (frontal zone) appear from the Philippine Sea to Japan along the western to northern peripheries of the subtropical anticyclone. Thus, the low-level moisture inflow into the YHRBs from the south is significantly reduced in the total field. The upper-level troposphere shows a north–south wavy flow in the midlatitude westerlies, including the Asian jet (Fig. 7b). An enhanced anticyclonic ridge extends from 30°N, 100°E to 60°N, 110°E and a deep trough can be seen to the east of the ridge, east of China. Convergent fields dominate over the YHRBs, reflecting subsidence that suppresses convection behind the deep trough. In phase 7, zonally elongated active convection (i.e., the mei-yu/baiu frontal zone) extends from the eastern Tibetan Plateau to Japan (Fig. 7c). Strong horizontal wind shear is observed over the key region. A subtropical anticyclone extends into the northern South China Sea, inducing strong southwesterly flow in the active convection band. This circulation structure causes convergence and maintains active convection over the YHRBs. In the upper-level troposphere (Fig. 7d), a shallow and wide trough appears from the eastern Tibetan Plateau to the east of Japan, with upper-level divergence to its southern flank, where convection is active.

Figure 8 shows the total convection and circulation series during 14–18 June 1989. Our aim is to understand how the midlatitude waves affect real weather systems on submonthly time scales over the YHRBs. In 1989, the NET pattern is highly dominant (Fig. 5a) and three active convection periods appear during the mei-yu period (Table 1). Each active period is associated with a similar atmospheric circulation field (not shown). Therefore, the convection and circulation series during 14–18 June 1989 can be regarded as a typical example of YHRB convection that is enhanced by the NET pattern. In Fig. 6, 14 June and 17–18 June correspond to phases 5 and 7, respectively. A band of convection moves southward from northeast of the Tibetan Plateau to southern China during this period (Figs. 8a–e). The southward movement of banded convection corresponds to that of a surface front over China, which is stationary, except on 15 June (Figs. 8f–j). Low-level horizontal

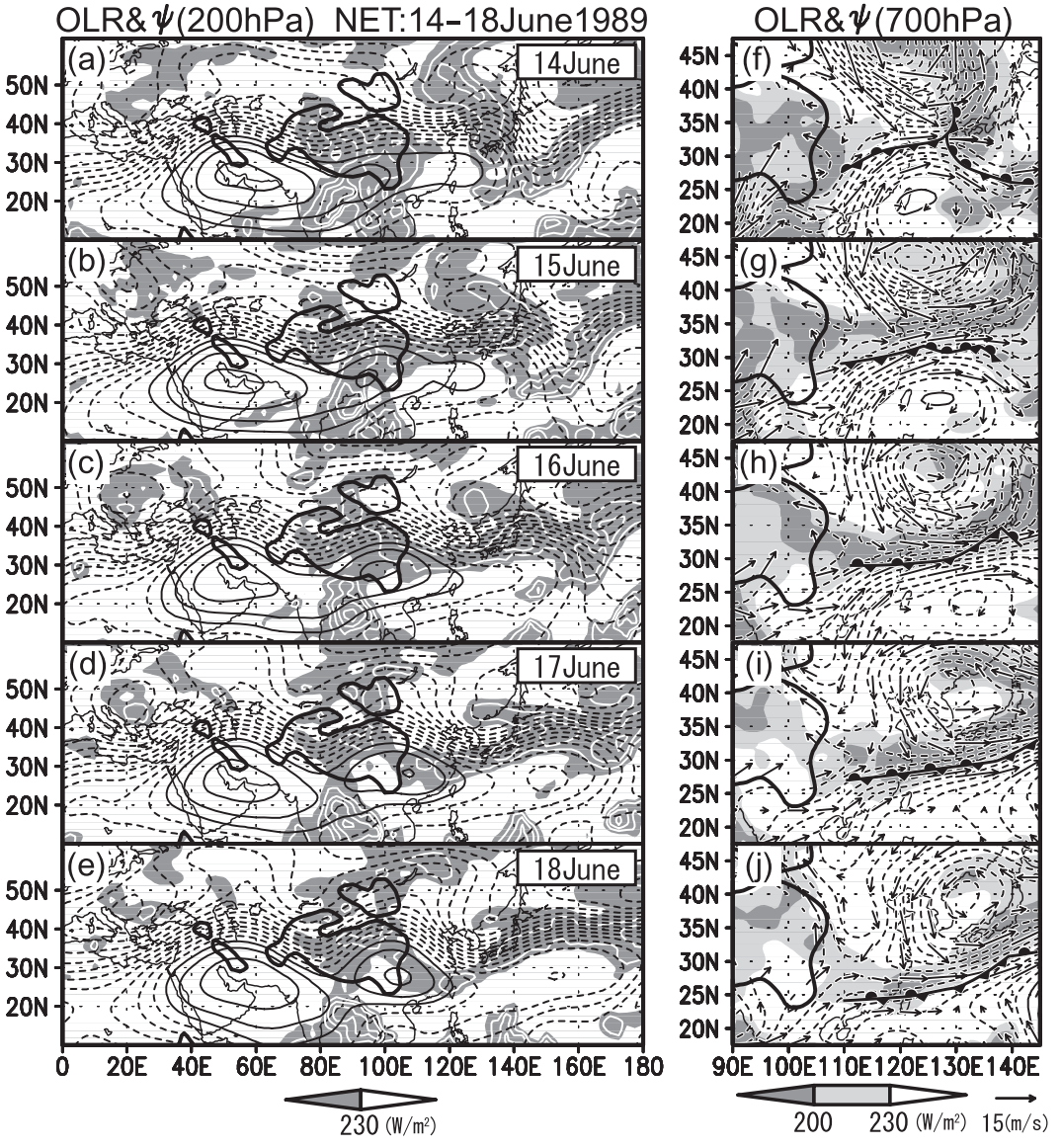

FIG. 8. (a)–(e) Spatiotemporal evolution of the 200-hPa total streamfunction (contours) and OLR (shadings) during 14–18 Jun 1989. The contour interval for streamfunction is 6.0×10^6 m^2 s^{-1}. OLR values less than 230 W m^{-2} are represented by shading. The contour interval for OLR (white contours) is 30 W m^{-2}. The thick solid line indicates the topographic contour line for 1500 m. (f)–(j) As in (a)–(e), but for 700 hPa, with the plots magnified only around the key region. The 700-hPa wind vector is also shown, and the position of a surface front is drawn from the surface weather chart of 1200 UTC for each day. The contour interval for streamfunction is 1.5×10^6 m^2 s^{-1}. The contour line for OLR is not drawn.

convergence (or wind shear) dominates along the banded active convection zone. In the upper-level troposphere, an enhanced ridge appears over the westerly jet around 40°N, 50°E on 14 June. At this time, a Tibetan high also develops to the west of the Tibetan Plateau (Fig. 8a). From 90° to 140°E, the westerly jet shows a nearly zonal structure. There is a trough around 50°N, 110°E, at a similar location to that in the lower troposphere, demonstrating a barotropic structure. The upper-level trough is located around 100°E on 8 June (not shown) and moves eastward very slowly. By 18 June, the westerly jet changes into the wavy state; there is clear downstream development of the wave around 40°N from 40° to 160°E, without marked phase propagation. Thus, the wave is quasi-stationary and has a zonal wavenumber of ~6. Associated with the downstream development, the upper-level trough develops around 45°N, 130°E on 15 June and deepens

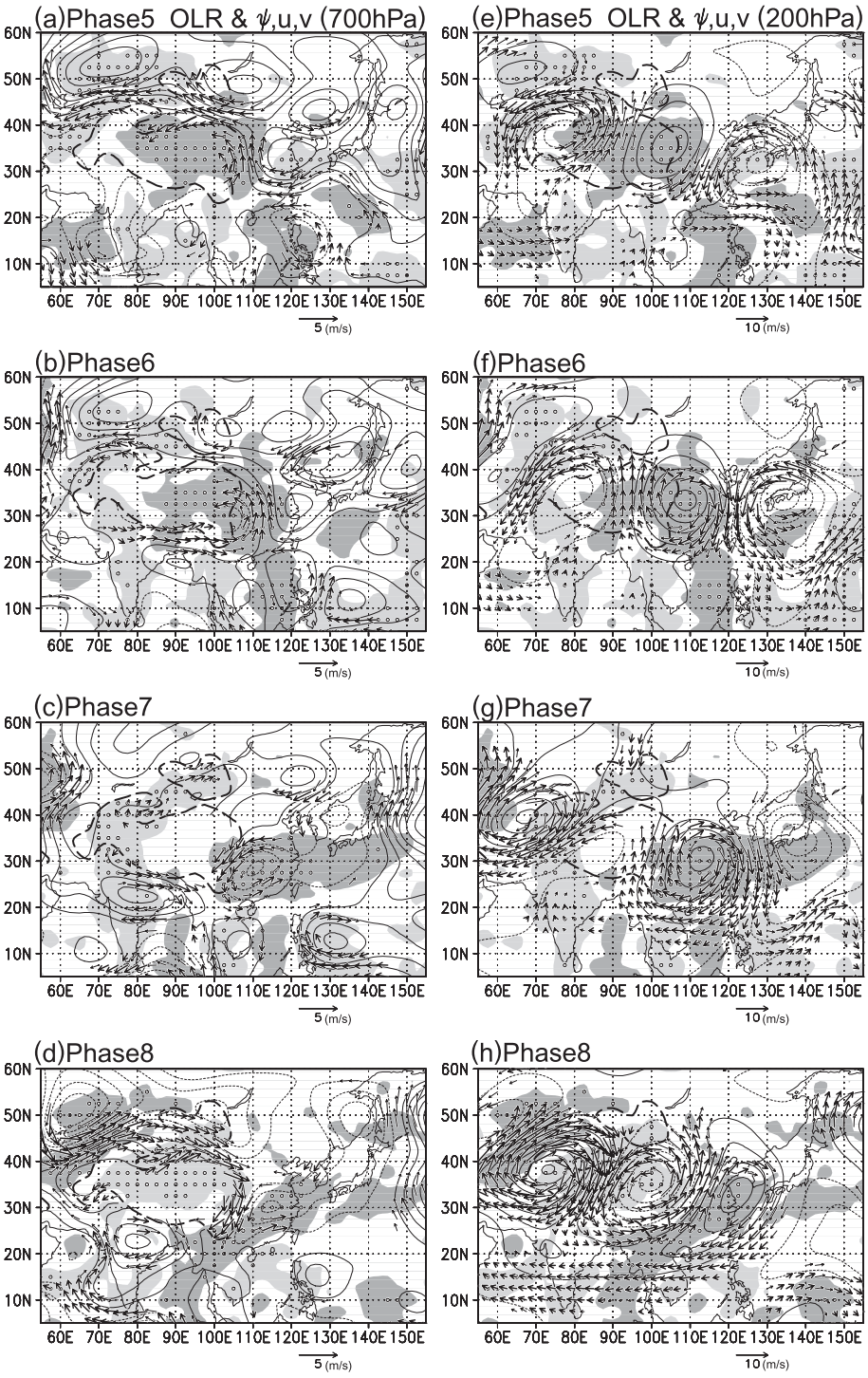

FIG. 9. As in Fig. 6, but for the AT pattern.

southward by 18 June. Thus, the southward amplification of the barotropic trough, due to the downstream development of the Rossby waves, causes the southward movement of the mei-yu front around the YHRBs in the NET pattern.

d. AT pattern

The development of OLR and atmospheric circulation in the AT pattern (Fig. 9) differs greatly from that in the NET pattern. From phases 5 to 7, eastward-moving

active OLR anomalies from the Tibetan Plateau to the YHRBs are evident (Figs. 9a–d, dark shading) at a mean speed of 3.7 m s^{-1} at 30°N. In phase 5 (Fig. 9a), an anticyclonic circulation anomaly is located over the YHRBs, with suppressed convection. In phase 6 (Fig. 9b), when the active convection anomalies reach the eastern flank of the Tibetan Plateau, a cyclonic anomaly develops there at 700 hPa, accompanied by significant southerly wind anomalies to its east. In phase 7 (Fig. 9c), a closed cyclonic anomaly is established over the key region and has the most active convection. By phase 8 (Fig. 9d), active convections show a northeastward tilt with a banded structure from the Indochina Peninsula to the YHRBs. From phase 7, suppressed convection anomalies appear over the western Tibetan Plateau and move eastward in the subsequent phases.

In the upper-level troposphere (right panels), a wave train extends from west of the Tibetan Plateau to Japan, crossing the plateau. In phase 5 (Fig. 9e), cyclonic circulation anomalies develop over the western Tibetan Plateau, centered on 38°N, 75°E. At 500 hPa, which corresponds to low-level atmosphere over the Tibetan Plateau, a center of cyclonic circulation is formed over the western Tibetan Plateau, similar to the location of such circulation at 200 hPa, but extending farther eastward to 100°E (not shown). The development of the trough induces a southerly flow of moist air toward the plateau, enhancing convection over it (e.g., FY04). By phase 6, the overall wave pattern moves slightly eastward at a mean eastward phase speed of 3.5 m s^{-1} at 35°N. Wave anomalies also grow downstream. Associated with this, the cyclonic circulation over the western Tibetan Plateau decays slightly, and anticyclonic circulation is strengthened over the eastern periphery of the plateau. In phase 7 (Fig. 9g), the anomalous anticyclone still remains over the YHRBs. Comparison of the anomaly signs between the low-level (Fig. 9c) and upper-level troposphere reveals that they are completely out of phase over the YHRBs. Active moist convection over the YHRBs induces upper-level divergence. To compensate, low-level convergence is also required. The mass compensation could be primarily responsible for the enhancement of low-level cyclonic circulation in the eastern part of the Tibetan Plateau, although the upper-level anticyclonic circulation above the cyclonic circulation is mainly due to the eastward movement of the upper-level wave train. The anomalous cyclone over the western Tibetan Plateau decays significantly, whereas an anticyclonic circulation anomaly develops rapidly over the western fringe of the Tibetan Plateau. By phase 8 (Fig. 9h), the signs of circulation anomalies near the Tibetan Plateau are completely reversed compared to those in phase 5 (Fig. 9e). The anomalous anticyclone is further strengthened over the western Tibetan Plateau, and an anomalous cyclone is established rapidly at the downstream side of the anomalous anticyclone. Southwest–northeast-banded convection lies to the east of the anomalous trough.

In the total field, in phase 3, convection is suppressed over the YHRBs, even though low-level southwesterlies flow into the southern regions of the basins (Fig. 10a). The mei-yu–baiu front covers an area from South China to Japan, with the most active region over Japan. Thus, the suppressed convection is not influenced by northwestern intrusion of the subtropical high, as in the NET pattern. In the upper-level circulation (Fig. 10b), large-scale convergence behind an upper-level trough is evident over a large area of the YHRBs, suggesting that subsidence suppresses convection. In phase 7 (Fig. 10c), the distribution of low-level southwesterlies flowing into the south of the key region is nearly the same as in phase 3, but the wind speed is greater. Cyclonic vorticity is dominant over the YHRBs, reflecting low-level convergence. The difference in the low-level flow pattern around the South China Sea between phases 3 and 7 is small compared to that in the NET pattern (Fig. 7). In the upper-level troposphere, anticyclonic circulation dominates, with divergence over the YHRBs (Fig. 10d).

Figure 11 shows a series of a typical AT pattern observed during 18–22 June 1993. The year 1993 is characterized by the highest variance of submonthly-scale variability in convection over the YHRBs (Fig. 2) and the predominance of the AT pattern (Fig. 5a). The three active periods of convection during the 1993 mei-yu period (Fig. 3c and Table 1) were induced by atmospheric circulations with a similar feature in each case. Therefore, the period 18–22 June was chosen as a typical example showing that the YHRBs convection is enhanced by the AT pattern. Maximum convection (i.e., phase 7) is found on 21 June over the YHRBs. On 18 June there is a banded active convection zone over south China (Fig. 11a), associated with a surface stationary front (Fig. 11f). There is also active convection over the Tibetan Plateau. From 19 to 20 June, the active convection over the plateau moves eastward to the YHRBs (Figs. 11b,c), where a surface low is generated at 30°N, 115°E along the stationary front (Figs. 11g,h). On 21 June, the surface low begins to move eastward with active convection, gaining in strength. The surface front over the YHRBs becomes cold on 21 June. It is located along a low-level convergence zone ahead of a closed cyclonic circulation at 700 hPa. The upper-level circulation contains a wavy jet at approximately 40°N on 18 June (Fig. 11a). The structure starts developing on 16 June (not shown). Ridges and troughs on the jet remain at almost the same position from 17 to 19 June,

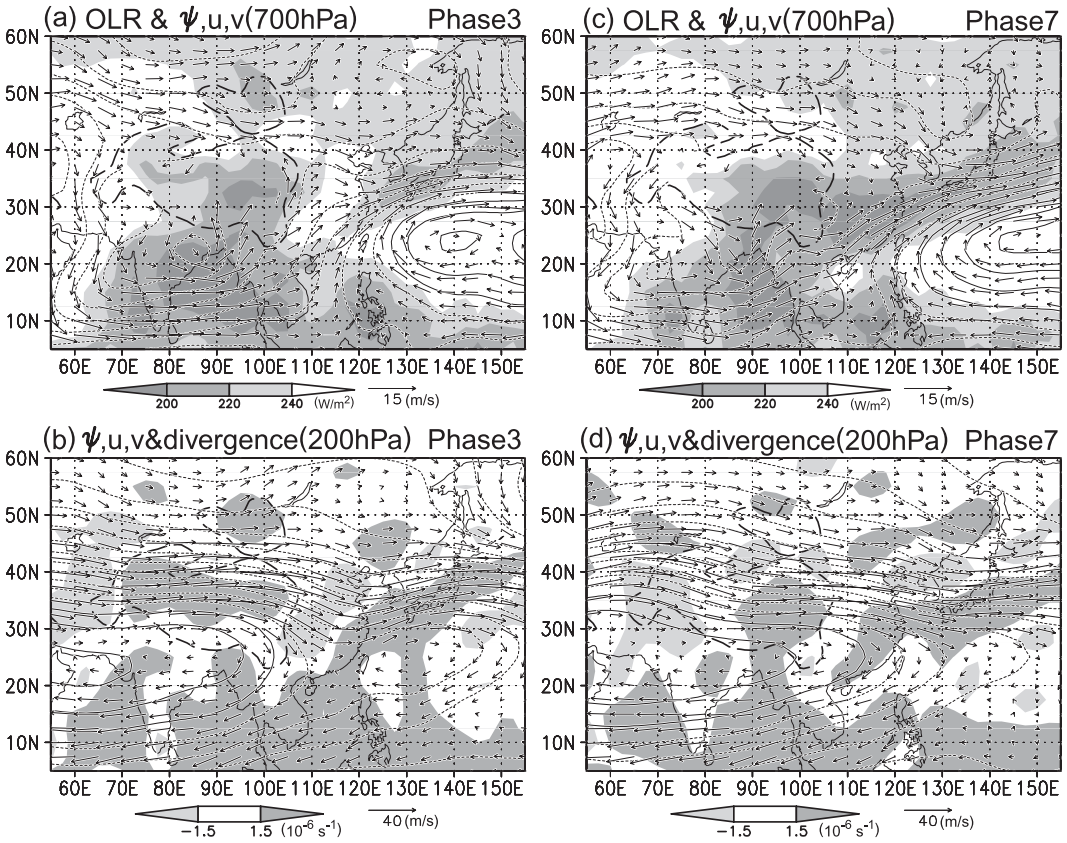

FIG. 10. As in Fig. 7, but for the AT pattern.

showing a characteristic of Rossby waves with zonal wavenumbers approximately 7–8. The vertical structure of the wave is barotropic to the north of 35°N by 19 June, but a vertical phase reversal becomes prominent over the YHRBs after 20 June, when the convection becomes active there. After 19 June, the overall wave structure at 40°N moves eastward at approximately 5.0 m s^{-1}. Simultaneously, a ridge appears and is strengthened over the YHRBs, accompanied by active convection. The wavy jet breaks into the relatively zonal jet structure on 21 June. The generation of a low-level vortex (or low) on the eastern flank of the Tibetan Plateau, probably due to the eastward propagation of Rossby waves with active convection over the plateau, is associated with the AT pattern.

5. Discussion

a. Effects of the background time-mean flow and the Tibetan Plateau on the two contrasting propagation patterns

The NET and AT propagation patterns are likely affected by the contrasting structures of the time-mean flow in the upper-level troposphere for each pattern. Figures 12a,b plot the time-averaged streamlines for the NET and AT patterns, respectively. The 5-yr averages of a 25-day low-pass-filtered u and v during the mei-yu period were used as the background flow for each pattern. A low-pass filter was applied to reduce the effects of high-frequency transients, including submonthly time scales, on the structure of the basic flow. The basic flows for the NET and AT patterns show statistically significant differences in the meridional wind around the Tibetan Plateau. In the NET pattern, which was associated with enhancement of the Tibetan high around the southern Tibetan Plateau, the axis of the westerly jet meanders northward in an arc from 80° to 120°E to the north of the plateau, showing a wavy-jet structure. The wavy background flow likely supports wave propagation along the northern flank of the Tibetan Plateau in NET pattern years. In contrast, the background westerly flow in the AT pattern shows a more zonal structure around the Tibetan Plateau, associated with the enhancement of the Tibetan high to the west of the plateau (Fig. 12b). The zonal jet provides favorable conditions for waves to propagate downstream across the Tibetan Plateau. The zonal wind speed is significantly larger than that in the NET pattern in upstream areas of the plateau. This

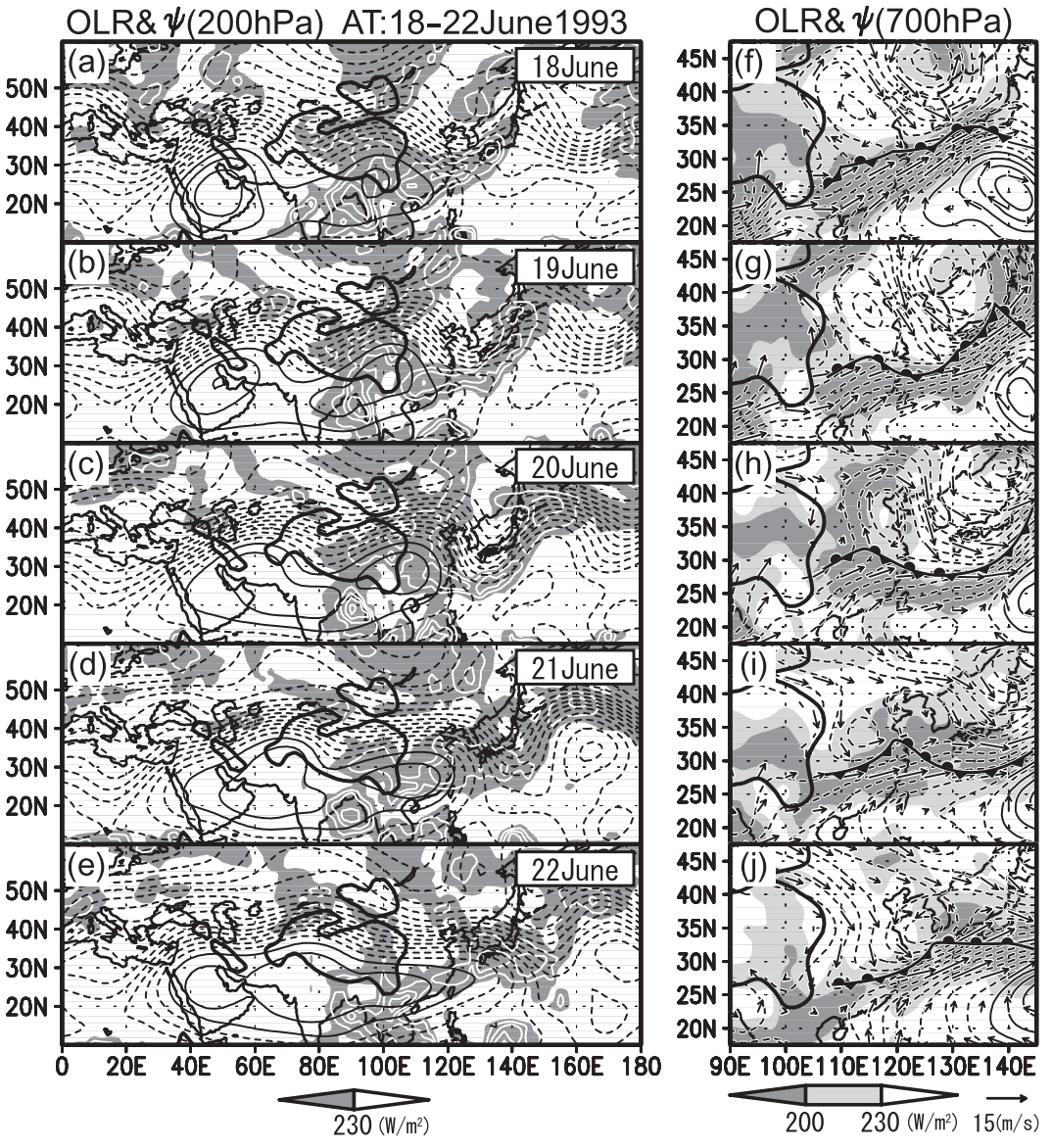

FIG. 11. As in Fig. 8, but for 18–22 Jun 1993.

might contribute to eastward movement of wave trains from the west of the plateau in the AT pattern. Thus, the contrasting structures of the background basic flow could cause the different propagation patterns of Rossby waves along the Asian jet around the plateau. In addition to the difference in the background basic flow around the plateau, the topography of the plateau may influence the alternation of the two wave propagation patterns. Topography might affect the northward arching time-mean flow around the plateau, creating amplification northward/northeastward through the dynamical action of the plateau. Further study is required to understand why the appearance of these wave trains is so closely correlated with the geography.

b. Characteristics of submonthly-scale midlatitude waves in the NET and AT patterns

As mentioned in the previous section, the midlatitude waves that affect submonthly convective variation over the YHRBs have Rossby wave characteristics. They are nearly barotropic to the north of the Tibetan Plateau in both patterns, although the vertical phase reversal becomes prominent to the east of the plateau in the AT pattern as convection intensifies over the YHRBs. The waves are also barotropic from 30° to 150°E to the north of the plateau (not shown). The waves in the NET pattern have an approximate wavenumber of 6, with an eastward phase speed of 0–2.5 m s^{-1} along 40°N (Figs.

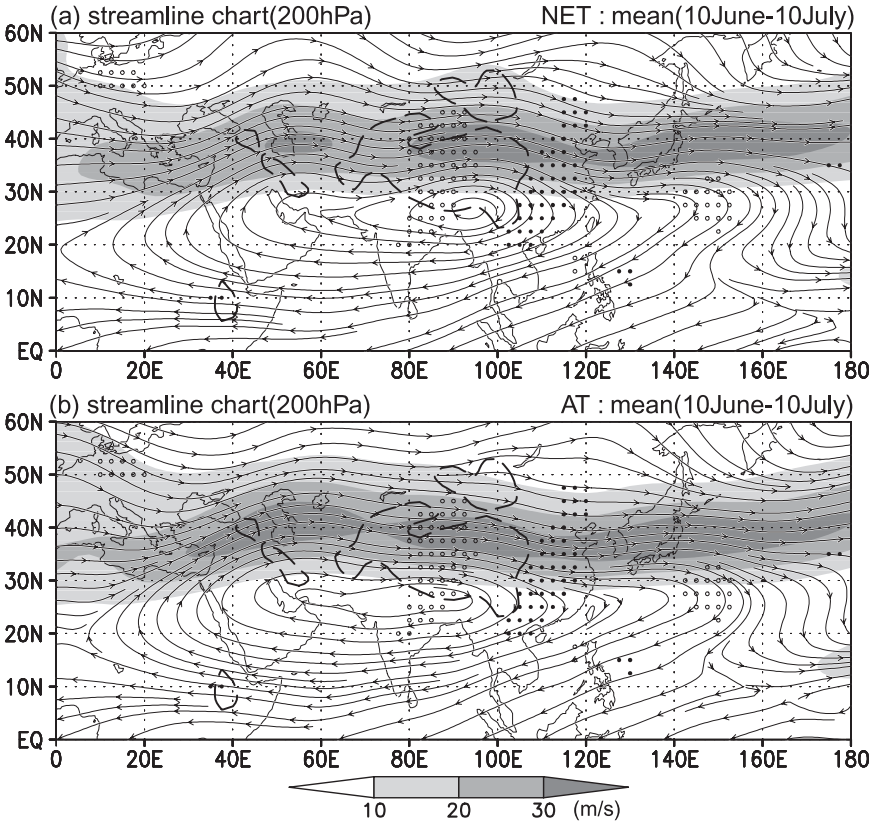

FIG. 12. Charts of the 200-hPa streamline constructed with 25-day low-pass-filtered wind during the mei-yu period (a) for the NET pattern and (b) for the AT pattern. Shadings denote areas more than 10 m s^{-1} in the zonal wind component. The thick dashed line denotes the 1500-m topographic contour line. Closed (open) circles denote grids of statistically significant negative (positive) difference at the 95% significance level in the low-pass-filtered meridional wind component between the NET and AT patterns.

6e–h and 8a–e). The waves in the AT pattern have wavenumbers of 7–8, with phase speeds of 3.5–5 m s^{-1} (Figs. 9e–h and 11a–e). The different phase speeds are probably the reason for the different directions of convection motion over the YHRBs, as well as for the difference in the mean basic state of the Asian jet. Here we qualitatively compare the theoretical phase velocity of a barotropic Rossby wave (e.g., Holton 1992) with observed results. The zonal phase speed relative to the background zonal wind speed is

$$c - \overline{u} = -\frac{\beta}{k^2 + l^2}, \qquad (1)$$

where c is the zonal phase speed; $\overline{u}$ is the background zonal wind speed; k and l are the zonal and meridional wavenumbers, respectively; and β is the meridional gradient of the Coriolis parameter. We can assume that the zonal and meridional wavenumbers are of similar scale ($k \approx l$) for midlatitude synoptic-scale disturbances (Holton 1992). The value of β is 1.75×10^{-11} m^{-1} s^{-1} at 40°N. In the NET pattern, the zonal wavenumber is 6. Hence, the Rossby wave speed relative to the background flow calculated from (1) is -5.6 m s^{-1}, whereas that in the AT pattern with wavenumber 7 is -4.1 m s^{-1}. Here, the background zonal wind for the barotropic Rossby waves is defined as the vertical mean 25-day low-pass-filtered zonal wind (from the lowest standard pressure level above the ground to 100 hPa), averaged over 30°–50°N, 80°–120°E, where the Rossby waves are observed. The background mean zonal flows are then 7.8 and 8.5 m s^{-1} in the NET and AT patterns, respectively. Hence, the phase speeds of the waves relative to the ground are 2.2 and 4.4 m s^{-1} in the NET and AT patterns, respectively. Although these values are rough estimates only, they agree well with the observed eastward phase speeds of the waves in the NET and AT patterns, respectively.

During the mei-yu period, the dominant period of ISOs in convection exhibits large interannual variation

over the YHRBs (see Fig. 2). This interannual variation likely depends on the upper-level waves around the YHRBs. It would be interesting in future research to examine the processes determining the dominant period of ISOs in midlatitude waves along the Asian jet during the mei-yu period.

c. *Effects of the Tibetan Plateau on submonthly convective variability over the YHRBs*

This study reveals that upper-level wave activities over the midlatitude westerly zone around the Tibetan Plateau have a significant impact on convective fluctuations at submonthly time scales over the YHRBs (Figs. 6–12). The Tibetan Plateau also plays an active role in the submonthly convective variability over the YHRBs. In the NET pattern, the topography of the plateau is important for convection. Low-level convergence between northerlies and southerlies is limited to the east of the plateau due to the Himalaya–Tibet massif. In the NET pattern, because the atmospheric circulation changes drastically from the north of the YHRBs, the low-level convergence starts in regions to the northeast of the plateau. Thus, the change in atmospheric circulation due to the midlatitude waves and the plateau topography creates favorable conditions for low-level convergence to the east of the Tibetan Plateau. In the AT pattern, both the plateau topography and the eastward movement of active convection and associated low-level atmospheric circulation over the plateau are important, before convection is enhanced over the YHRBs (e.g., Figs. 9a and 11a,b). Although we did not examine the detailed enhancement process of the low-level vortex to the east of the plateau, some previous studies presented plausible hypotheses. Yasunari and Miwa (2006) showed that, when the active convection and associated convergence zone reaches over the eastern edge of the plateau, cyclogenesis is induced by vertical stretching of the vortex due to downslope movement on the eastern edge of the plateau and to latent heating due to convection. The submonthly-scale midlatitude waves do affect the location of the active convection and associated convergence zone over the Tibetan Plateau (e.g., Figs. 9e–h and 11a–e). The development of the upper-level trough over the western Tibetan Plateau (Figs. 9e and 11a,b) causes the enhancement of convection from the central to eastern parts of the plateau because low-level humid southerlies toward the plateau are strengthened ahead of the trough (cf. FY04). Thus, the slow eastward movement of the midlatitude waves and the enhancement of convections over the Tibetan Plateau are probably essential for the genesis of low-level vortices in the AT pattern.

6. Summary

We examined convective variability at submonthly time scales (7–25 days) over the YHRBs and the associated large-scale atmospheric circulation during the mei-yu season (10 June–10 July), using OLR and NCEP–NCAR reanalysis data for the period from 1979 to 2004. The 7–25-day filtered OLR anomalies averaged over the key region (25°–35°N, 110°–120°E) were used as an index to study submonthly variation over the YHRBs. The fluctuation of OLR anomalies was closely associated with the activities of the quasi-stationary (mei-yu) front and embedded mesoscale vortex, or low. We found two contrasting relationships between convection in the YHRBs and the midlatitude waves along the Asian jet. Results are summarized as follows:

1) The variance in submonthly-scale convective fluctuation over the YHRBs shows large interannual variation. Submonthly-scale convective variability is notable during the mei-yu season in 1981, 1985, 1986, 1989, 1992, 1993, 1995, 2000, 2001, 2002, 2003, and 2004.
2) Correlations between the convection index and upper-level circulation during the mei-yu season reveals two contrasting patterns: one with positive (negative) correlations to the north (south) of the key region (e.g., 1981, 1985, 1989, 1992, and 2004), and the other with negative correlations over the entire key region (e.g., 1986, 1993, 1995, 2001, and 2003). In the former pattern, high correlations extend along the northern to eastern peripheries of the Tibetan Plateau with an arclike structure (defined as ''NET''). In the latter pattern, high correlations appear across the Tibetan Plateau, with a wave train–like structure (defined as ''AT'').
3) Composite analyses indicate quite different spatiotemporal structures in the NET and AT patterns, even though YHRBs convection fluctuations are the same on submonthly time scales. Composites of the NET pattern show that convection anomalies migrate southward slowly from the northeastern periphery of the Tibetan Plateau to South China and have a zonally oriented southwest–northeast tilt, which corresponds to the southward migration of a surface quasi-stationary front (mei-yu front). The initiation and development of the active (inactive) convection anomalies is induced by the development of cyclonic (anticyclonic) circulation anomalies to the north of the key region in both the upper and lower troposphere. The southward migration of the cyclonic (anticyclonic) circulation anomalies from the north causes active (inactive) convection anomalies.
4) In contrast, the composite sequence for the AT pattern shows that convection anomalies migrate eastward

from the western Tibetan Plateau to the YHRBs. When the active (inactive) convection anomalies reach the eastern flank of the Tibetan Plateau, a cyclonic (anticyclonic) anomaly rapidly develops there at 700 hPa, and upper-level circulation shows an anticyclonic (cyclonic) anomaly over the key region. The atmospheric structure between the Tibetan Plateau and the YHRBs in the AT pattern provides favorable conditions for the genesis of a low-level mesoscale vortex or low at the eastern edge of the plateau. The eastward migration of convection anomalies is due to that of upper-level circulation anomalies along the Asian jet.

5) In the total fields, during the active extreme of YHRB convection in both the NET and AT patterns, a strong low-level southerly-southwesterly wind carries abundant moisture into the YHRBs and its convergence yields active convection over the YHRBs. Although upper-level circulation features contrast in the NET and AT patterns, upper-level divergence dominates over the active convection regions in both patterns. In the inactive phase, tropospheric subsidence associated with upper-level convergence behind an upper-level trough is a major suppressor of YHRB convection in both patterns. In the lower troposphere, southerly-southwesterly flow is significantly weakened in the NET pattern, whereas in the AT pattern, southerly-southwesterly flow dominates over the southern part of the YHRBs.
6) In both the patterns, the midlatitude wave trains play a crucial role in regulating the YHRB convection on submonthly time scales. The waves are Rossby-like, with the NET pattern having an approximate wavenumber of 6 and 0–2.5 m s^{-1} eastward phase speed relative to the earth's surface and the AT pattern having a wavenumber of 7–8 and eastward phase speed of 3.5 to 5.0 m s^{-1}. In addition, the mean basic state of the Asian jet is significantly different around the Tibetan Plateau between the two patterns. The Asian jet has wavy characteristics in the NET pattern, with a northward arclike structure around the plateau. This structure may help develop large-amplitude waves to the north-northeast of the plateau. The zonal jet structure is more dominant in the AT pattern, creating a condition in which midlatitude waves pass eastward over the plateau. Thus, these differences probably lead to the differences in convection anomaly behavior over the YHRBs between the two patterns.

Acknowledgments. We thank Prof. K. Nakamura and Prof. H. Uyeda of Nagoya University and other members of the Lower Atmosphere and Precipitation Study (LAPS)/Core Research for Evolutional Science and Technology (CREST) project for their many constructive comments and suggestions. Thanks are also extended to Dr. K. Tuboki of Nagoya University, Dr. T. Terao of Kagawa University, and Dr. Y. Fukutomi of the Frontier Research Center for Global Change (FRCGC) for their many insightful comments. This study was partially supported by the CREST program of the Japan Science and Technology Agency (JST) and a Grant-in-Aid for Young Scientists (B-20740268) from the Japanese Ministry of Education, Culture, Sports, Science, and Technology.

REFERENCES

Ambrizzi, T., B. J. Hoskins, and H.-H. Hsu, 1995: Rossby wave propagation and teleconnection patterns in the austral winter. *J. Atmos. Sci.,* **52,** 3661–3672.

Chen, G. T.-J., 2004: Research on the phenomena of Meiyu during the past quarter century: An overview. *East Asian Monsoon*, C.-P. Chan, Ed., World Scientific, 357–403.

Chen, T.-C., M.-C. Yen, and S.-P. Weng, 2000: Interaction between the summer monsoons in East Asia and the South China Sea: Intraseasonal monsoon modes. *J. Atmos. Sci.,* **57,** 1373–1392.

Ding, Y., 1992: Summer monsoon rainfall in China. *J. Meteor. Soc. Japan,* **70,** 373–396.

——, and J. C. L. Chan, 2005: The East Asian summer monsoon: An overview. *Meteor. Atmos. Phys.,* **89,** 117–142.

Duchon, C. E., 1979: Lanczos filtering in one and two dimensions. *J. Appl. Meteor.,* **18,** 1016–1022.

Enomoto, T., B. J. Hoskins, and Y. Matsuda, 2003: The formation mechanism of the Bonin high in August. *Quart. J. Roy. Meteor. Soc.,* **129,** 157–178.

Fujinami, H., and T. Yasunari, 2004: Submonthly variability of convection and circulation over and around the Tibetan Plateau during the boreal summer. *J. Meteor. Soc. Japan,* **82,** 1545–1564.

Fukutomi, Y., and T. Yasunari, 1999: 10–25 day intraseasonal variations of convection and circulation over East Asia and western North Pacific during early summer. *J. Meteor. Soc. Japan,* **77,** 753–769.

——, and ——, 2002: Tropical-extratropical interaction associated with the 10–25-day oscillation over the western Pacific during the Northern summer. *J. Meteor. Soc. Japan,* **80,** 311–331.

Glickman, T., Ed., 2000: *Glossary of Meteorology*. 2nd ed. Amer. Meteor. Soc., 855 pp.

Holton, J. R., Ed., 1992: Atmospheric oscillations: Linear perturbation theory. *An Introduction to Dynamic Meteorology*, Academic Press, 183–226.

Hsu, H.-H., 2005: East Asian monsoon. *Intraseasonal Variability in the Atmosphere–Ocean Climate System,* K. M. Lau and D. E. Waliser, Eds., Springer, 63–94.

Kalnay, E., and Coauthors, 1996: The NCEP/NCAR 40-Year Reanalysis Project. *Bull. Amer. Meteor. Soc.,* **77,** 437–471.

Liebmann, B., and C. A. Smith, 1996: Description of a complete (interpolated) outgoing longwave radiation dataset. *Bull. Amer. Meteor. Soc.,* **77,** 1275–1277.

Madden, R. A., and P. R. Julian, 1972: Description of global-scale circulation cells in the tropics with a 40–50 day period. *J. Atmos. Sci.,* **29,** 1109–1123.

——, and ——,1994: Observations of the 40–50-day tropical oscillation: A review. *Mon. Wea. Rev.,* **122,** 814–837.

Mao, J. Y., and J. C. L. Chan, 2005: Intraseasonal variability of the South China Sea summer monsoon. *J. Climate,* **18,** 2388–2402.

——, and G. X. Wu, 2006: Intraseasonal variations of the Yangtze rainfall and its related atmospheric circulation features during the 1991 summer. *Climate Dyn.,* **27,** 815–830.

Matthews, A. J., and G. N. Kiladis, 1999a: Interactions between ENSO, transient circulation, and tropical convection over the Pacific. *J. Climate,* **12,** 3062–3086.

——, and ——, 1999b: The tropical–extratropical interaction between high-frequency transients and the Madden–Julian oscillation. *Mon. Wea. Rev.,* **127,** 661–677.

Ninomiya, K., 1984: Characteristics of Baiu front as a predominant sub-tropical front in the summer Northern Hemisphere. *J. Meteor. Soc. Japan,* **62,** 880–894.

——, and H. Muraki, 1986: Large-scale circulations over East Asia during Baiu period of 1979. *J. Meteor. Soc. Japan,* **64,** 409–429.

Takahashi, H., 2003: Observational study on the initial formation process of the Mei-yu frontal disturbance in the eastern foot of the Tibetan Plateau in middle-late June 1992. *J. Meteor. Soc. Japan,* **81,** 1303–1327.

Tao, S. Y., and Y. Ding, 1981: Observational evidence of the influence of the Qinghai-Xizang (Tibet) Plateau on the occurrence of heavy rain and severe convective storms in China. *Bull. Amer. Meteor. Soc.,* **62,** 23–30.

Terao, T., 1998: Barotropic disturbances on intraseasonal time scales observed in the midlatitudes over the Eurasian continent during the northern summer. *J. Meteor. Soc. Japan,* **76,** 419–436.

Tian, S.-F., and T. Yasunari, 1998: Climatological aspects and mechanism of spring persistent rains over Central China. *J. Meteor. Soc. Japan,* **76,** 57–71.

Torrence, C., and G. P. Compo, 1998: A practical guide to wavelet analysis. *Bull. Amer. Meteor. Soc.,* **79,** 61–78.

Ueda, H., and T. Yasunari, 1996: Maturing process of the summer monsoon over the Western North Pacific—A coupled ocean/atmosphere system. *J. Meteor. Soc. Japan,* **74,** 493–508.

Vincent, D. G., A. Fink, J. M. Schrage, and P. Speth, 1998: High- and low-frequency intraseasonal variance of OLR on annual and ENSO timescales. *J. Climate,* **11,** 968–986.

Wang, B., 1987: The development mechanism for Tibetan Plateau warm vortices. *J. Atmos. Sci.,* **44,** 2978–2994.

——, and I. Orlanski, 1987: Study of a heavy rain vortex formed over the eastern flank of the Tibetan Plateau. *Mon. Wea. Rev.,* **115,** 1370–1393.

Wang, W., Y.-H. Kuo, and T. T. Warner, 1993: A diabatically driven mesoscale vortex in the lee of the Tibetan Plateau. *Mon. Wea. Rev.,* **121,** 2542–2561.

Xie, P., A. Yatagai, M. Chen, T. Hayasaka, Y. Fukushima, C. Liu, and Y. Song, 2007: A gauge-based analysis of daily precipitation over East Asia. *J. Hydrometeor.,* **8,** 607–626.

Yasunari, T., and T. Miwa, 2006: Convective cloud systems over the Tibetan Plateau and their impact on meso-scale disturbances in the Meiyu/Baiu frontal zone—A case study in 1998. *J. Meteor. Soc. Japan,* **84,** 783–803.

Zhu, C. W., T. Nakazawa, J. P. Li, and L. X. Chen, 2003: The 30–60 day intraseasonal oscillation over the western North Pacific Ocean and its impacts on summer flooding in China during 1998. *Geophys. Res. Lett.,* **30,** 1952, doi:10.1029/2003GL017817.